Ground Fault Detector for DC Microgrids Using Sequentially-Switched Grounding Connections

José Manuel Guerrero, *Member, IEEE*, Itxaso Aranzabal, Julen Gómez-Cornejo, Pablo Eguía, *Member, IEEE*, Sergio Zarate, and Carlos A. Platero, *Senior Member, IEEE*

***Abstract*—With the increasing demand of renewable energy and recent research in smart Direct Current (DC) microgrids, electric systems with high presence of power electronics are gaining momentum. One piece of evidence is the emergence of ungrounded low voltage DC (LVDC) microgrids and their energy management, which are crucial for achieving high efficiency systems. However, they are difficult to protect against electrical faults, especially against Ground Faults (GF), due to the commutation frequencies and the duality of AC and DC currents that cause a lack of selectivity in conventional protection relays. In this paper a GF detection method is proposed for addressing this issue. The method discerns between the affected zone (AC or DC) by sequentially switching a grounding resistor among the different neutrals and DC midpoints of the system. The method is based on the frequency domain analysis of the voltage waveform measured on this grounding resistor. Afterwards, in the case of AC fault, the phase-to-neutral voltages in the affected zone are measured and compared with the voltage across the grounding resistor to identify the faulty phase. In the case of DC faults, the polarity of this last voltage also allows the identification of the faulty pole. To validate the method, numerous simulations and experimental tests have been performed obtaining satisfactory results.**

***Index Terms*—DC microgrids, grounding, fault current limiters, fault detection, voltage measurement, switching circuits.**

NOMENCLATURE

C	DC capacitor.
C_p	Parasitic capacitance.
f_0	DC component.
f_1, f_3	1st and 3rd AC grid harmonic frequency.
$f_{dj,k}$	Frequency of the drive "j" for a "k" harmonic.
f_k	"k" harmonic frequency.
φ_k	"k" harmonic phase angle.
I_{Cp}	Parasitic current.
I_f	Fault current.
L_f	Inductive filter.
R_1, R_2	Artificial midpoint resistors and resistances.
R_f	Fault resistance.
R_{gnd}	Grounding resistor and resistance.
U_{if_k}	Fault potential amplitude in the electrical point "i" for the "k" harmonic.
U_{if}	Fault potential in the electrical point "i".
U_{in}	Phase "i"-to-neutral voltages.
U_{DC}	DC bus voltage.
U_{gnd}	Grounding resistor voltage.
x	Fault position.
Z	Load impedance.
Z_{L1}, Z_{L2}	Line impedance.
Δ_{td}	Dead time between switches.

Manuscript received 8 January 2024; revised 17 April 2024; accepted 31 July 2024. Date of publication 20 August 2024; date of current version 15 November 2024. Paper 2023-IDC-2002.R1, presented at the 2023 IEEE International Conference on Environment and Electrical Engineering and 2023 IEEE Industrial and Commercial Power Systems Europe, Madrid, Spain, Jun. 06–09, and approved for publication in the IEEE TRANSACTIONS ON INDUSTRY APPLICATIONS by the Industrial Drives Committee of the IEEE Industry Applications Society [DOI: 10.1109/EEEIC/ICPSEurope57605.2023.10194616]. This work was supported in part by Basque Government and in part by GISEL research group (Universidad del Pas Vasco) under Grant OT1522-22. *(Corresponding author: Carlos A. Platero.)*

José Manuel Guerrero, Itxaso Aranzabal, Julen Gómez-Cornejo, and Pablo Eguía are with the Electric Engineering Department, Universidad del País Vasco, 48014 Bilbao, Spain (e-mail: josemanuel.guerrerog@ehu.eus; itxaso.aranzabal@ehu.eus; julen.gcb@ehu.eus; pablo.eguia@ehu.eus).

Sergio Zarate is with the Electronics and Computing Department, Mondragon Unibertsitatea, 20500 Arrasate, Spain (e-mail: szarate@mondragon.edu).

Carlos A. Platero is with the Automatic, Electric and Electronic Engineering and Industrial Computing Department, Universidad Politécnica de Madrid, 28003 Madrid, Spain (e-mail: carlosa.platero@upm.es).

Color versions of one or more figures in this article are available at https://doi.org/10.1109/TIA.2024.3446749.

Digital Object Identifier 10.1109/TIA.2024.3446749

I. INTRODUCTION

POWER electronics are key elements in power systems for the efficient control of electric energy. They are commonly used to integrate renewable generation into grids and even to operate the grid itself. For instance, power converters are commonly utilized in low voltage (LV) microgrids, where usually a common Direct Current (DC) bus ensembles all the drives, generators and grid connections. These systems are increasingly being adopted in buildings, cities and even in electric transportation due to their exceptional energy management capacity [1].

The proliferation of power converter is experiencing exponential growth, as evidenced indirectly in the Electric Vehicle (EV) sector expansion [2] and in the increasing production of renewable energy [3]. However, with this increase, the probability of electric faults is also growing. The voltage pulses used by the electronic elements lead to a premature degradation of the insulation of drives and cables causing electrical faults [4]. The most common type of faults in power systems, and even more in converter-based systems, are Ground Faults (GFs) [5], which are produced by this insulation degradation.

LVDC microgrids grounding configurations are varied [6]. Among the most common groundings, the solidly grounded, the high resistance grounded (HRG), low resistance grounded

(LRG) and ungrounded configurations are the most used. Most of LVDC microgrids are commonly ungrounded. Then, a first GF should not cause any damage since there are no fault currents. HRG and also LRG can be used to considerably limit the fault current and achieve higher protection sensitivity. A lower grounding resistance will make protection relays more sensitive to the fault current. However, a second GF could cause devastating damages. In this field, many studies have been developed in DC microgrids [7], [8], photovoltaic (PV) power plants [9], variable speed drives [10], [11], [12], traction power systems [13], and other related areas.

The use of commercial protection relays is not recommended for protecting DC microgrids. GFs could occur in the AC sides or DC sides of the grid. In this way, the protection relays could malfunction due to the appearance of an unexpected type of current in its measurement device. For example, current transformers of AC differential relays could saturate if faults occur in the DC side of the grid [12]. To address this issue, extensive coordination of multiple protection relays is required [14]. Additionally, commutation frequencies of power electronics could cause a lack of selectivity in the protection relays, e.g., in overcurrent relays [15].

For this reason, numerous protection methods, schemes and systems have been developed to protect DC microgrids. In [7], [8] currents are measured at the midpoints installed at each end of each line of the DC microgrids. These midpoints are formed by capacitors. Since this grounding is limited by a current limiting impedance, when a GF occurs, the transient measured at the grounded terminals makes possible the DC fault location. However, the grounded system can malfunction due to faults in the AC sides provoking undesirable fault currents. Additionally, high frequency currents will flow among the different connections. With the same grounding connection, PV wiring can also be protected [9]. In order to protect this DC part, in [16], a cooperative control of the converters for the GF protection has been proposed for rigid or low impedance capacitor-grounded microgrids.

Other alternative techniques widely extended in the fault diagnosis are based on Artificial Neural Networks (ANN) and artificial intelligence techniques. Thanks to this approach, an algorithm can be trained by performing extensive simulations and collecting system measurements data. Then, if the real-time measured data deviates from healthy state, it implies a fault. In case of having trained the algorithm with multiple faults, the methods could classify, detect the zone, distinguish between a maneuver or a GF transient, or even locate the fault [17], [18], [19], [20].

Also, the AC drives connected to DC microgrids are key pieces of the system. Their insulation aging is faster than in conventional AC loads due to the high gradients caused during their voltage/current modulation. Therefore, their protection is essential. GFs could be monitored performing off-line insulation tests. In this field, [21] proposes some useful tests to monitor the stator of inverter-driven electrical machines. In this case, the inverter itself acts as a monitoring device. In [22], the stator of EV motors is monitored using zero-sequence voltage component as a fault indicator. It allows to perform diagnosis during the machine's operation. Another technique for this purpose is the analysis of the stator current signatures [23], [24]. Some methods provide additional fault information, such as the one presented in [25]. In that case, both sides of an AC/AC drive are considered to detect the faulty phase of the controlled motor. The faulty phase can be identified by observing angle variations between the current in an artificial neutral point in the AC controlled side and the current in the grid side grounding.

Furthermore, there are methods that address the duality of the problem and detect both AC and DC faults inside a variable speed drive. In [10], a grounding resistor is placed in the neutral of the main power transformer of an AC/AC drive. It enables the detection of the fault zone by analyzing the frequency components of the voltage measured at the grounding resistor. If these systems have a low impedance grounding, they can also be protected using a toroidal differential relay in the secondary of the power transformer [12]. However, the exact faulty zone cannot be identified. Moreover, DC faults could saturate the toroid. Other methods consider the use of DC midpoints formed with two capacitors or high-value resistors to detect GFs, e.g., in [26], this method is used in railway electrical traction systems, where the GF is detected by measuring the DC midpoint voltage displacement and data-driven methods.

These methods are crucial for protecting power converter-based systems from faults and to implement fault location methods. An example is given in [11] for the variable speed drive AC zone of an AC/AC system.

In all the previous methods, the grounding was performed using a current limiting resistor in one or more fixed points of the system. Commonly, the power transformer's neutral has a high value resistance grounding. It allows a constant monitoring of faults even in a steady state. Nevertheless, in case of multiple AC zones with the same frequency or multiple DC zones, the faulty drive cannot be identified. In case of having multiple DC midpoints grounded, most of them are capacitive with low value current limiting resistors. It implies that only a transient analysis can be performed. Another problem of this type of multiple static grounding is that both AC and unbalanced currents also flow through these points.

In this paper, a method for GF detection in DC microgrids with multiple AC/DC converters is proposed. The method sequentially connects and disconnects a single point high value grounding resistor at different neutral and midpoints of the microgrid. Thereby the fault current path varies. This alternative avoids undesirable returning currents through different grounded points. Furthermore, the midpoints are considered resistive in order to enable the steady-state fault monitoring. Subsequently, by analyzing the voltage measured across this grounding resistor for each commutation position, the method can identify the specific zone in the microgrid where the fault is taking place. The method works even if some drives are operating at the same fundamental and commutation frequencies or even if the microgrid has different connection points to the main power system. Additionally, by measuring the phase-to-neutral voltage of the AC zones and comparing it with the grounding resistor voltage, the faulty phase can be identified. The method

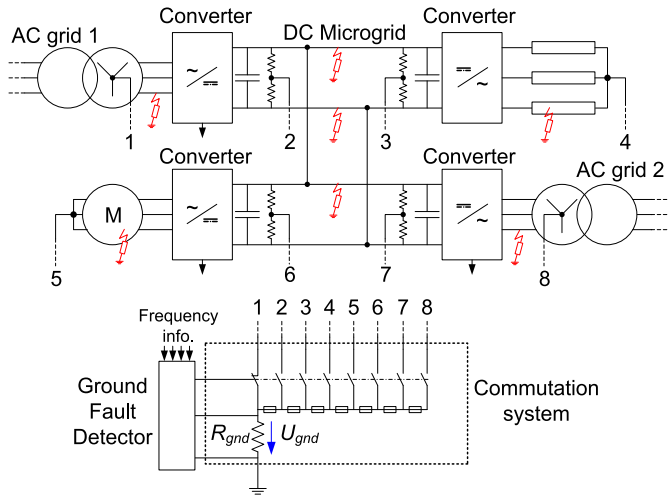

Fig. 1. Example of DC microgrid with the proposed GF detector and grounding connection installation.

was previously and briefly presented at a conference in [27] and it was granted a Spanish Patent [28].

This paper is structured as follows: Section II introduces the operation principles of the detection method. Next, Section III describes the simulation model, and Section IV analyzes the results. Likewise, Section V presents the experimental setup, and Section VI analyzes the experimental results. Finally, Section VII provides the main contributions of the manuscript and concludes the paper.

II. Operating Principles of the Ground Fault Detection Method

In this section, the operating principles of the proposed GF detection method are explained. The method is based on installing a grounding resistor, R_{gnd}, in the AC neutrals and DC midpoints of the system. In the case of star connection of the drives or transformers, the neutral is accessible, and a connection can be easily extracted. If the neutral is not accessible, an artificial one can be used. To access the midpoints, voltage dividers with high-value resistors can be installed. Fig. 1 shows an example of these neutrals and midpoints connections. This figure presents an example of microgrid with 2 grid connections and 2 drives connected to a common DC bus that will be used as case study.

Once the midpoints and neutrals are obtained, they are all connected to a commutation system. This system has a switch for each neutral/midpoint connection which connects them with R_{gnd} and then with the ground. The voltage U_{gnd} is measured to monitor the state of the power system.

In the commutation system, one of the switching elements should be normally closed, while the rest must remain open in order to avoid short circuits. Fuses are strongly recommended to prevent damages in case of commutation failures.

In the case of a healthy state operation, no fault current, I_f, will flow through R_{gnd}. It implies that U_{gnd} will be null or will have low voltage values due to parasitic capacitive currents, I_{Cp}, as shown in (1):

$$I_f + I_{Cp} = I_{Cp} = -\frac{U_{gnd}}{R_{gnd}} \tag{1}$$

In (1), the opposite polarity of U_{gnd} measurement regarding I_f causes the negative sign (see it in Figs. 1 or 2). However, when a fault exists, the fault current flows through R_{gnd} obtaining a U_{gnd} value different from 0 V:

$$I_f = -\frac{U_{gnd}}{R_{gnd}} = \frac{U_{if}}{R_f + R_{gnd}} \tag{2}$$

where U_{if} is the potential difference between the faulty point "*i*" and the DC midpoint/ AC neutral grounding.

In case of artificial DC midpoints, the resistive voltage divider should be considered in the fault path as:

$$U_{gnd} = -\frac{R_{gnd}}{R_{gnd} + R_f + \frac{R_1 R_2}{R_1 + R_2}} \cdot U_{if} \tag{3}$$

In (2) and (3), I_{Cp} is neglected as the parasitic capacitances, C_p, are in parallel with the fault resistance, R_f, which has a considerably lower value.

At the event of a fault, the switches should be sequentially commutated, varying the I_f returning paths among the different neutrals and midpoints. By consequence, U_{if} will be changing attending to the grounding position as well. Therefore, different U_{gnd} waveforms will be registered. With the high value of R_{gnd}, the imaginary part of the impedances involved in the circuit can also be neglected. Thus, U_{gnd} will have the same features than I_f and U_{if}. For different harmonics, it can be stated in (4) as:

$$U_{gnd}\ (f_k) = -\frac{R_{gnd}}{R_f + R_{gnd}} U_{if}\ (f_k) \tag{4}$$

Different waveform possibilities can occur depending on the grounding connection. As shown in Fig. 2(a), if the fault is in the same side as the commutation element is switched ON, neither U_{if} nor U_{gnd} will not present high frequency harmonics. It is because there are not power converters involved in the fault circuit. The clearest example can be given for a DC fault when the DC switch is closed. Equation (5) shows it:

$$U_{gnd} = -\frac{R_{gnd}}{R_{gnd} + R_f + \frac{R_1 R_2}{R_1 + R_2}} \cdot \left(x - \frac{1}{2}\right) U_{DC} \tag{5}$$

where x is the fault position and it is 0 for negative pole faults and 1 for positive pole faults. In the case of Fig. 2(a), $x = 0$. In case of an AC fault, $x = 0$ in the neutral of the AC load and 1 in terminals of the converter.

However, if the grounding connection is switched ON in a different zone, at least one converter is involved in the fault circuit. It means that U_{gnd} will have at least the commutation frequency of the affected converter (see Fig. 2(b)). In this case, the power converter can be substituted by an AC source with its produced harmonics. The representative example of Fig. 2(b) can be summarized in the following U_{gnd} expression:

$$u_{gnd}\ (t) = -\frac{R_{gnd}}{R_{gnd} + R_f} \cdot \left(x - \frac{1}{2}\right) U_{DC}$$

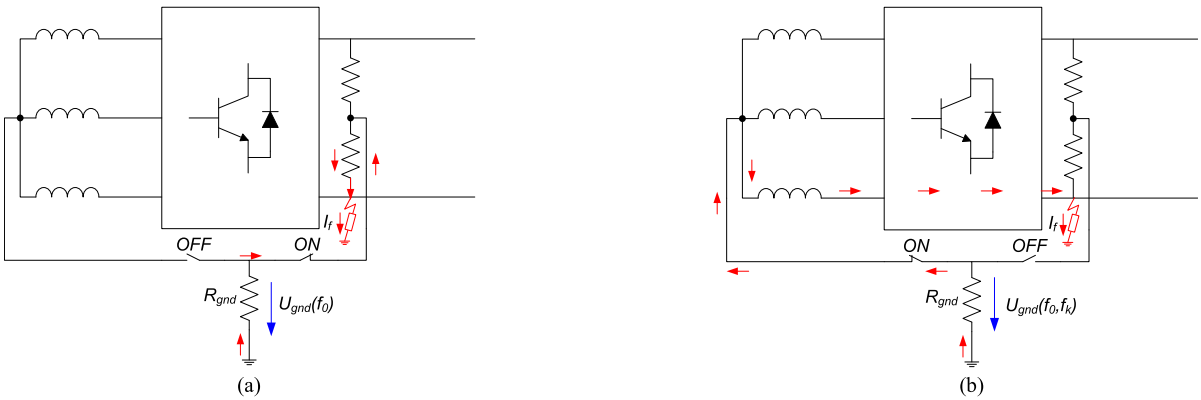

Fig. 2. Theoretical fault in a DC side [(a): R_{gnd} connected in the midpoint point of the faulty zone; (b): R_{gnd} connected in the neutral of a healthy zone].

$$+\sum_{k=2}^{\infty}\frac{R_{gnd}}{R_{gnd}+R_f}\cdot U_{if\_k}e^{j(2\pi f_k t+\varphi_k)} \quad (6)$$

where u_{if_k} is the amplitude of the faulty point voltage respect to the neutral point in the "k" harmonic produced by the converter involved. In case of more power converters involved, more waveform summations should be added with their respective harmonics. Analogous equations can be extracted for other grounding and fault positions.

Then, performing a Fast Fourier Transform (FFT) in the U_{gnd} measurements, the different U_{gnd} harmonics can be extracted for each R_{gnd} grounding position. In this way, the faulty zone will be located as the zone where U_{gnd} measurement has the lowest commutation harmonic frequency.

Another evidence of the presence of a fault is given when the fundamental frequency measured in U_{gnd} corresponds with the faulty drive frequency (0 Hz in case of DC faults). Furthermore, in case of a fault in the DC side, if some midpoints are accessible, the fault location can be bounded nearer to the connection that presents the higher U_{gnd} (f_0) measurement.

With this procedure, if some drives have the same operation settings, the fault can be discerned, addressing the issues encountered by other methods such as in [10]. Additionally, faults on the DC side can also be identified.

It must be observed that, to start the diagnosis process, one of the switches must be normally closed. Once a high value of U_{gnd} is detected, the diagnosis process starts. During the healthy state, the grounding must be switched regularly in order to avoid lack of selectivity produced if the GF is very closed to the grounded point. The threshold must be studied by the operator in order to reach more or less sensitivity to ground faults considering (3) for DC midpoints and (4) for AC neutrals. To summarize the fault detection method, Fig. 3 maps a synthetized flowchart. A final protection trip can be added at the end of the fault detection process.

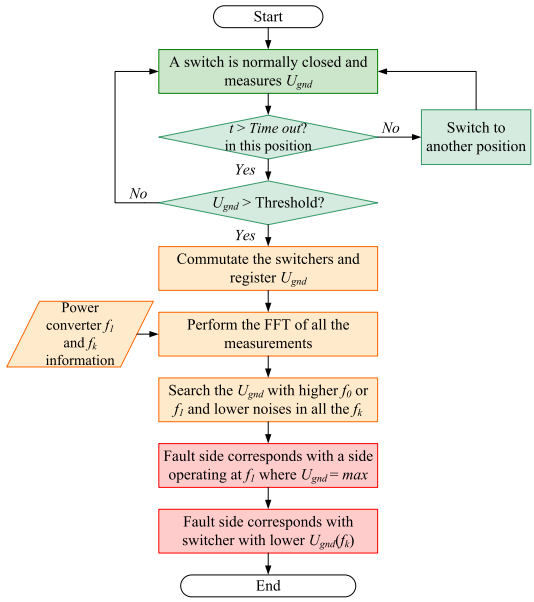

Fig. 3. Flowchart of the proposed ground fault detection method.

III. Simulation Model

To validate the proposed method, several simulations have been performed in Matlab Simulink. The simulation model is presented in detail in Fig. 4. This model emulates the circuit shown previously in Fig. 1. It consists of two grid connections and two AC drives connected to the same DC bus or microgrid.

The grids have been modeled with 400 V - 50 Hz balanced three-phase voltage sources with a 3 mH filter, L_f, before the converters. Both converters are controlled to maintain 650 V in the DC bus. If the voltage exceeds the specified limit, the excess of energy is fed back to grid and vice versa.

On the DC side, a 1638 μF capacitor is connected to the terminals of each grid converter. Two breakers are used to connect the converter to the rest of the DC grid when the rated voltage is reached. Then, three cables are considered. For the connection from grid 1 to drive 1, and likewise from grid 2 to drive 2, the wires impedances are $Z_{L1} = 1 + \mathrm{j}\omega{\cdot}120 \times 10^{-6}\ \Omega$. The wire connecting grid 1 to grid 2 has an impedance of $Z_{L2} = 20 + \mathrm{j}\omega{\cdot}2.4 \times 10^{-3}\ \Omega$.

On the other side, two converters, that feed two variable speed drives, are placed. Both converters operate as PWM controllers, managing the fundamental and commutation frequencies of

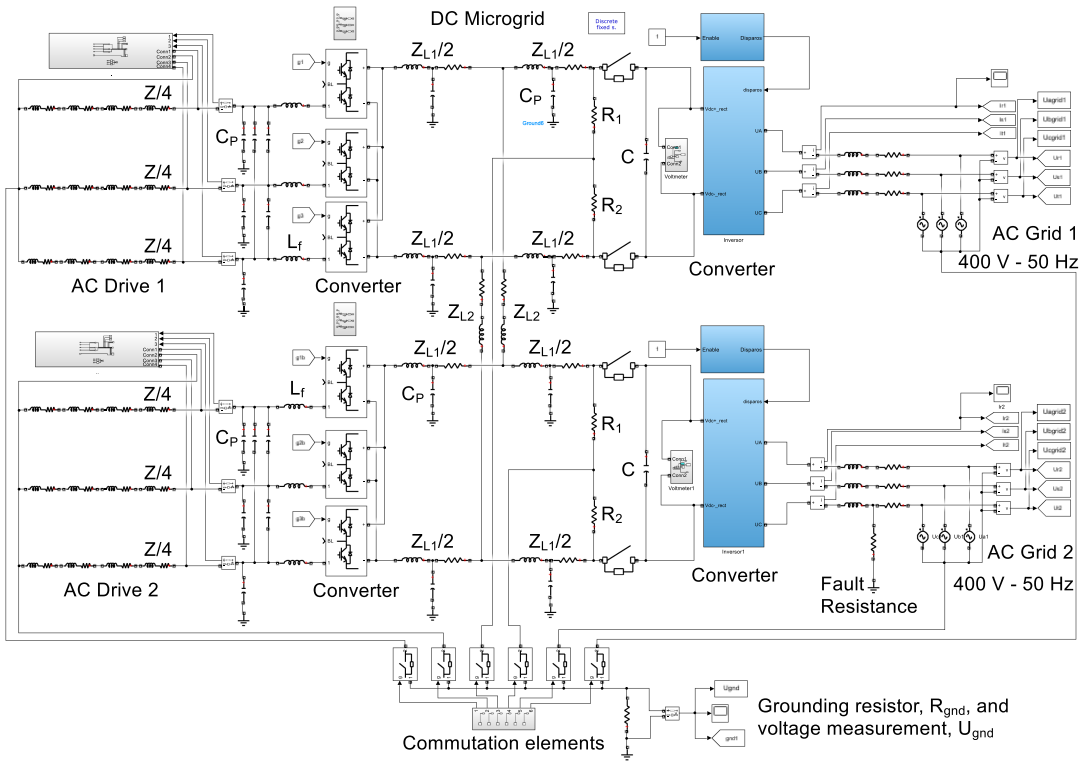

Fig. 4. Simulation model.

drives 1 and 2. The fundamental frequencies are $f_1 = 20$ Hz and 40 Hz, while the commutation frequencies are $f_k = 5$ kHz and 10 kHz, respectively. On the AC side of the inverters, fractional RL loads simulate two identical variable speed drives with an impedance of $Z = 50 + \mathrm{j}\omega{\cdot}20 \times 10^{-6}\ \Omega$. Inductive filters of 3 mH have been placed before the drives to reduce the current's noise.

Additionally, mutual and phase-to-ground parasitic impedances, C_p, of 0.1 and 0.25 pF have been considered in the circuit. These parameters are important to observe the effect of parasitic currents during healthy operation, especially at high frequencies.

In this system, the neutrals and artificial DC midpoints (formed by $R_1 = R_2 = 4.7$ kΩ) are connected to commutation elements. The commutation elements are switched sequentially with a driving time of 50 ms and a dead time, Δt_d, between two adjacent switches of 10 ms. The other terminal of the commutation elements is connected to a high-value grounding resistor $R_{gnd} = 4.7$ kΩ which limits the fault current to a maximum of 50 mA. In R_{gnd}, the voltage U_{gnd} is measured and monitored. In Fig. 4, an example of GF can be seen, which is simulated as a resistive fault (R_f) in the AC grid 2.

IV. Simulation Results

A healthy state scenario and GFs in different locations of the power system with different fault resistances have been simulated.

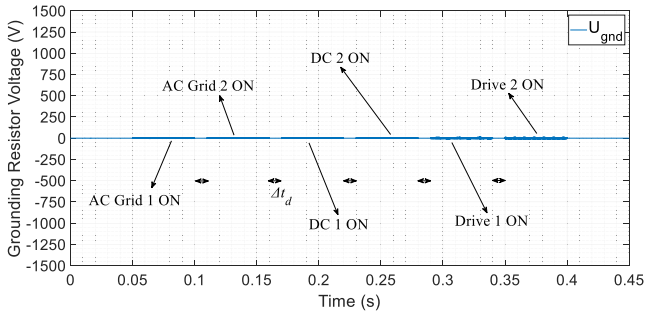

Fig. 5. Healthy state operation simulation.

A. Healthy State Simulation

Under healthy conditions, no GF exists. Therefore, $I_f = 0$ A and the voltage measured in R_{gnd} should be null. Fig. 5 shows a simulation carried out under these operating conditions. As shown, U_{gnd} is near zero due to the presence of parasitic currents.

B. Ground Fault Simulations

To analyze the location behavior in the proposed method, several GFs have been performed at different points of the simulated circuit also varying their R_f. The switching sequency has been carried out as follows: AC grid 1 neutral, AC grid 2 neutral, DC upper converter midpoint, DC lower converter midpoint, AC drive 1 neutral and AC drive 2 neutral.

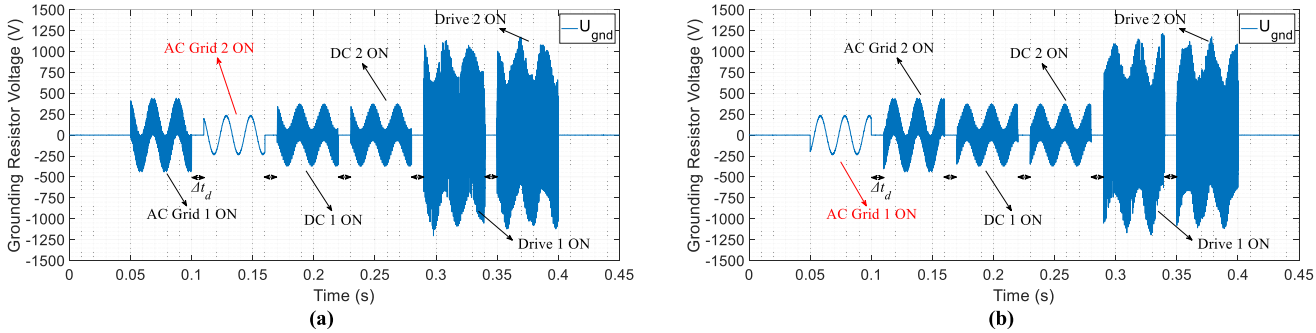

Fig. 6. AC grid side faults simulations [(a): AC grid 2 fault with $R_f = 0\ \Omega$; (b): AC grid 1 fault with $R_f = 0\ \Omega$].

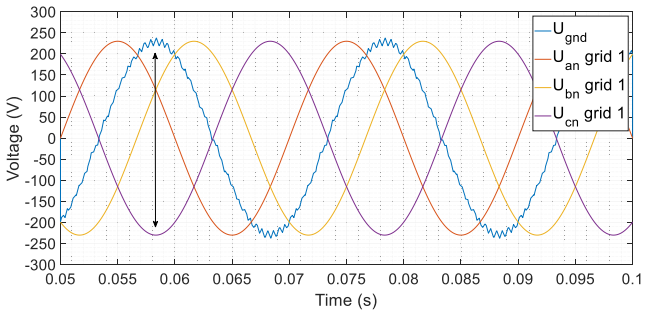

Fig. 7. AC grid 1 fault with $R_f = 0\ \Omega$ in phase "c"; U_{an}, U_{bn}, U_{cn} phase-to-neutral voltages compared with U_{gnd}.

Faults were provoked in the AC grid 1 and 2, AC drives 1 and 2, as well as in the poles (+) and (—) of the DC bus, with $R_f = 0\ \Omega$. Fig. 6(a) shows a fault in the AC grid 2 position as it is the only one that does not present commutation frequencies on its measure. Fig. 6(b) shows a fault in the AC grid 1 position. If only the voltage in R_{gnd} is measured, the information about the faulty phase is lost. As previous stated by the authors in [11], the phase-to-neutral voltages of the faulty side should be measured to obtain the AC phase with fault. This voltage will be at 180° with U_{gnd}. This is validated in Fig. 7, where U_{gnd} is out of phase with U_{cn}, indicating that the faulty phase is phase "c". Fig. 8 shows the FFT results of all the U_{gnd} windows for the case of Fig. 6(b). In this figure, only the AC grid 1 does not present high frequency components due to commutation elements, which is a clear indicator of where the fault is.

For faults in the DC side, the simulations results show DC components of U_{gnd} for all the measurements. Only the positions of DC midpoints have reduced high frequency noises. AC grids and drives neutrals provide DC component, but also, they have large commutation components. Fig. 9(a) depicts a fault in the DC (+) pole of the upper wire that connects AC grid 1 with drive 1. Fig. 9(b) depicts a fault in the DC (—) pole of the lower wire that connects AC grid 2 with drive 2. As has been proven, U_{gnd} will have opposite polarity to the pole in fault. Finally, Fig. 10 shows the frequency domain spectra of the DC (—) pole fault. Owing to the large values of R_{gnd} and the artificial midpoint resistors (R_1 and R_2), it is challenging to determine the exact location of the fault within the DC side, as all the DC side measurements are very similar.

Finally, the GFs are performed in AC drives 1 and 2. Figs. 11(a) and 12(a) show the results for a fault performed in the AC drive 1, while Figs. 11(b) and 12(b) show the fault performed in the drive 2. Both cases present some similarities. First, when the switching position is in the corresponding drive, the noise content is considerably reduced. For a fault in the AC drive 1, the commutation frequency of 5 kHz appears in all the measurements except in the AC drive 1 switching. Instead of 5 kHz, subharmonics, k, of 5 kHz $\pm$ 20 kHz appear on both sides of the 5 kHz harmonic. The same effect occurs for a fault in the AC drive 2, where all the measurements present 10 kHz harmonics except during the AC drive 2 switching position, that presents 10 kHz $\pm$ 40·k Hz. Thus, if the algorithm only focuses on the commutation frequency, the affected zone does not exhibit it while the others do. Regarding the faulty phase, the principle of counterphase also affects the AC drives. When phase-to-neutral voltages in the AC drives are compared to U_{gnd}, as it is shown in Fig. 13. In this figure, phase difference of 180° between both voltages is obtained. In this case, the faulty phase is the phase "c" of the AC drive 2.

To study the effect of R_f on the measurements, Fig. 9(a) can be compared with Fig. 14, where R_f is varied among the values: 2.2 kΩ, 4.7 kΩ and 10 kΩ. They approximately correspond to 50%, 100 % and 200 % of the grounding resistor value, respectively. In this regard, the authors have observed that the voltage value decreases from −214.26 V ($R_f = 0\ \Omega$) to −88.73 V (R_f = 10 kΩ), that nearly corresponds with the theoretical approach of a voltage divider between R_{gnd}, R_f and artificial midpoint resistors, R_1 and R_2, as stated in (5).

R_1 and R_2 are the reason why the measurements at the DC midpoints are more attenuated than those at the neutral. Despite the attenuation, the voltage still has a considerable value, which implies that the method is sensitive to GFs with high R_f. However, with the current configuration, the method does not locate or bound the fault resistance on the DC side.

In the case of having DC loads, generators or energy storage systems connected to the microgrid via DC/DC converter, the fault diagnosis could be performed following the same procedure.

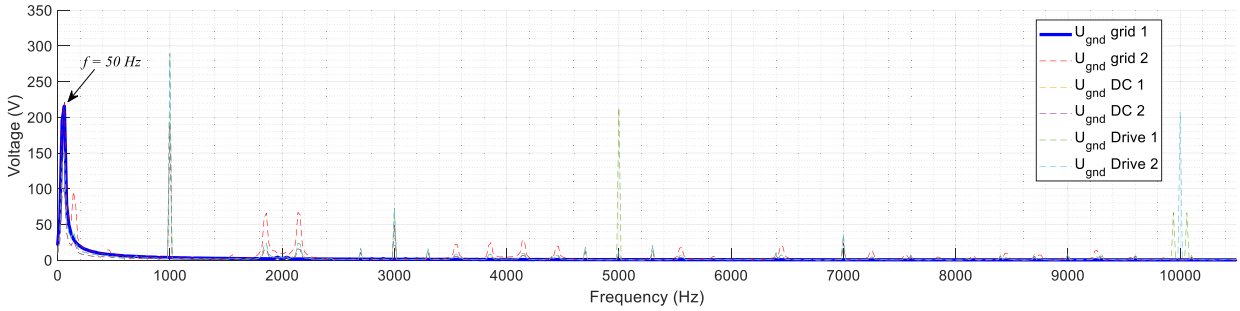

Fig. 8. FFT results of U_{gnd} simulations for each of the switching positions for a fault in the AC grid 1 side.

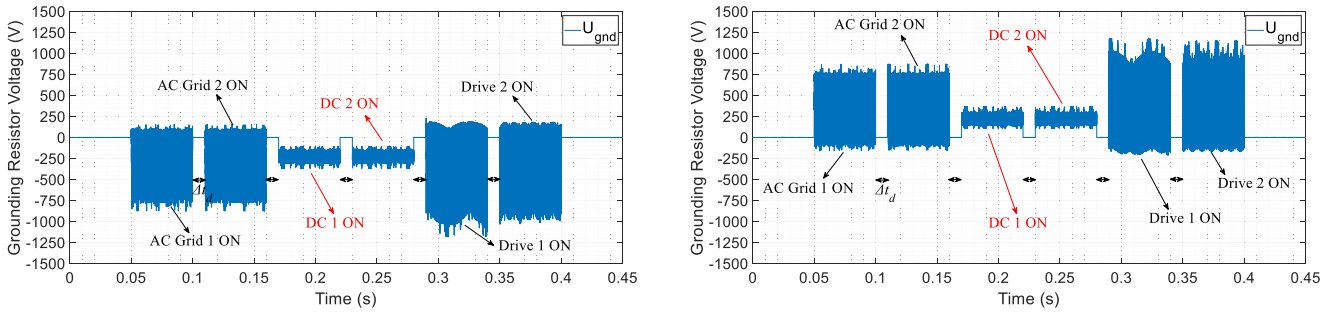

Fig. 9. DC faults side faults simulations [(a): DC positive pole fault in the AC grid 1 – AC drive 1 wire connection with $R_f = 0\ \Omega$; (b): DC negative pole fault in the AC grid 2 – AC drive 2 wire connection with $R_f = 0\ \Omega$].

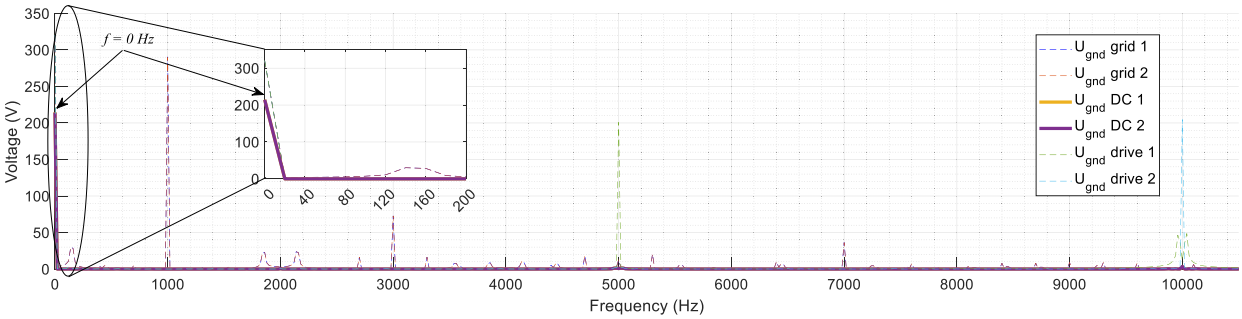

Fig. 10. FFT results of U_{gnd} simulations for each of the switching positions for a fault in the DC (-) pole fault of the AC grid 2 – AC drive 2 wire connection.

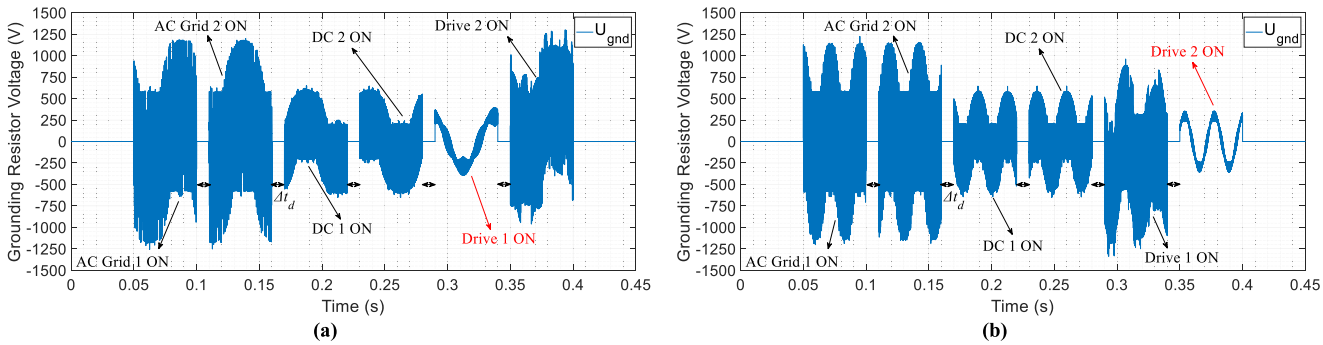

Fig. 11. AC drive side faults simulations [(a): AC drive 1 fault with $R_f = 0\ \Omega$; (b): AC drive 2 fault with $R_f = 0\ \Omega$].

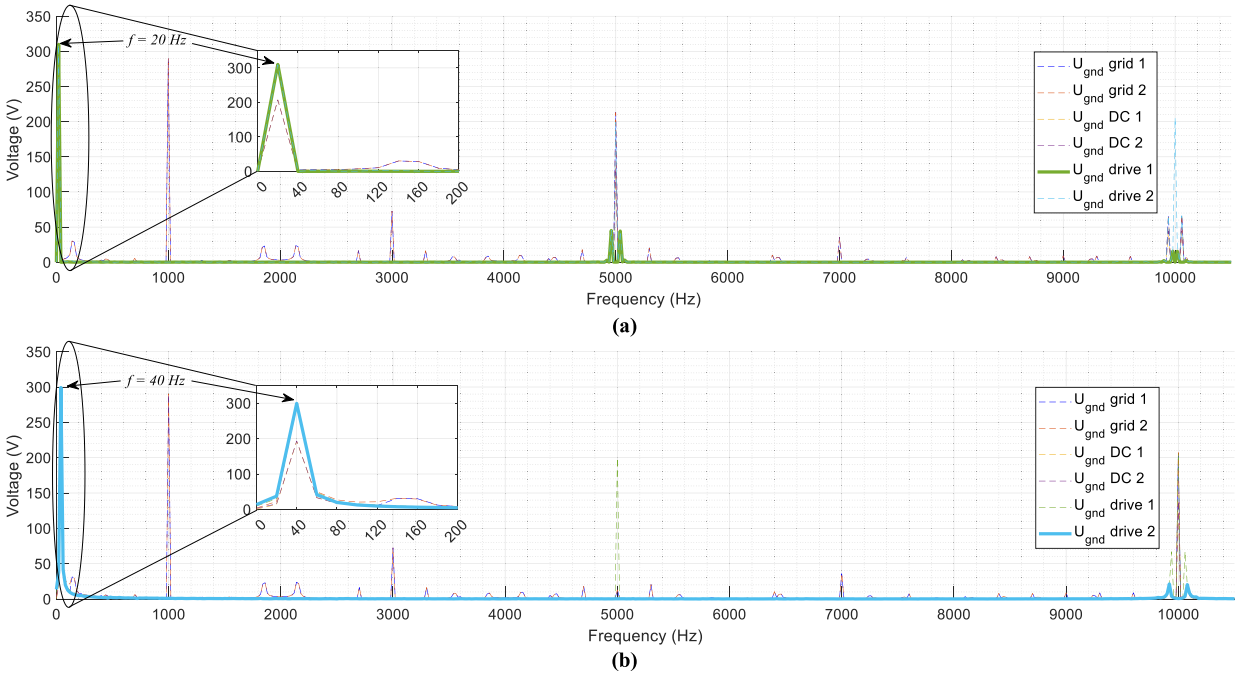

Fig. 12. FFT results of U_{gnd} simulations for each of the switching positions for a fault in the AC drive sides [(a): AC drive 1; (b): AC drive 2].

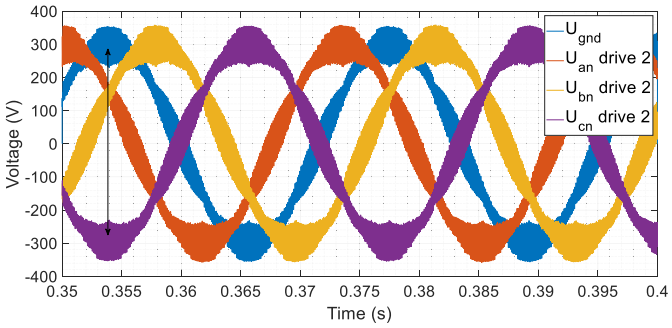

Fig. 13. AC drive 2 fault in phase "c" with $R_f = 0\ \Omega$: angle comparison between U_{an}, U_{bn}, U_{cn} and U_{gnd}.

V. Experimental Setup

To validate the simulations and methodology, an experimental setup emulating a DC microgrid with two drives and two AC grid (400 V / 50 Hz) interconnections has been built (see Figs. 15 and 16).

As shown in Figs. 15 and 16, the experimental setup consists of an AC grid interconnection (1) with two different 5.5 kW power transformers (2) 400/400 V that feed two frequency converters (3) of 5.5 kW and 7.5 kW rated power. The power converters have 6-pulses non-controlled rectifiers and 6-pulses IGBT-based inverters with accessible DC bus. A DC interconnection (4) was built between converters (3) from the DC bus, emulating a long cable with a resistance of $R = 10\ \Omega$. The 7.5 kW inverter terminals are connected to a 1.5 kW induction machine (IM), called AC drive 1 (6). This drive operates at a main frequency of $f_{d1,1} = 10$ Hz. On the other hand, the 5.5 kW inverter terminals has been connected to a passive RL load of $Z = 50\ \Omega + j\omega \cdot 4 \cdot 10^{-3}\ \Omega$ divided into four equal parts, AC drive 2 (5). In this second drive, the main operating frequency has been set at $f_{d2,1} = 42.5$ Hz. The commutation frequency of both drives is the same, $f_k = 5950$ Hz

The switching device has been placed in (7) to interconnect all the neutral points and artificial midpoints shown in Fig. 16. The commutation time will be 50 ms, with a dead time of 10 ms between commutations to avoid short-circuits between different parts of the experimental setup. The DC midpoints have been created using $R_1 = R_2 = 4.7$ kΩ. R_{gnd} also acquires this value, which limits the current up to 58 mA in case of a $R_f = 0$ fault on the DC side (most severe fault case). Furthermore, R_f of 0, 2.2, 4.7 and 10 kΩ are used in experimental tests. All these resistances are collected in (8) and (9). Finally, the voltage has been measured using a Yokogawa PZ4000 Power Analyzer (10) for 0.4 s and 0.45 s during different faults with 1 MS acquisition frequency. The data was then collected in a computer (11) for frequency analysis.

VI. Experimental Results

Different scenarios have been evaluated using the setup of Fig. 15. They are a healthy state test and GF tests with $R_f = 0$, 2.2, 4.7 and 10 kΩ at secondary of both transformers (AC grid 1 and 2 faults), DC (+) and (-) poles in different parts of the DC bus and AC drives 1 and 2. Some of the cases are shown below.

A. Healthy State Tests

Firstly, to validate the selectivity of the method, a healthy state test was performed (see Fig. 17). From this data, it is shown that

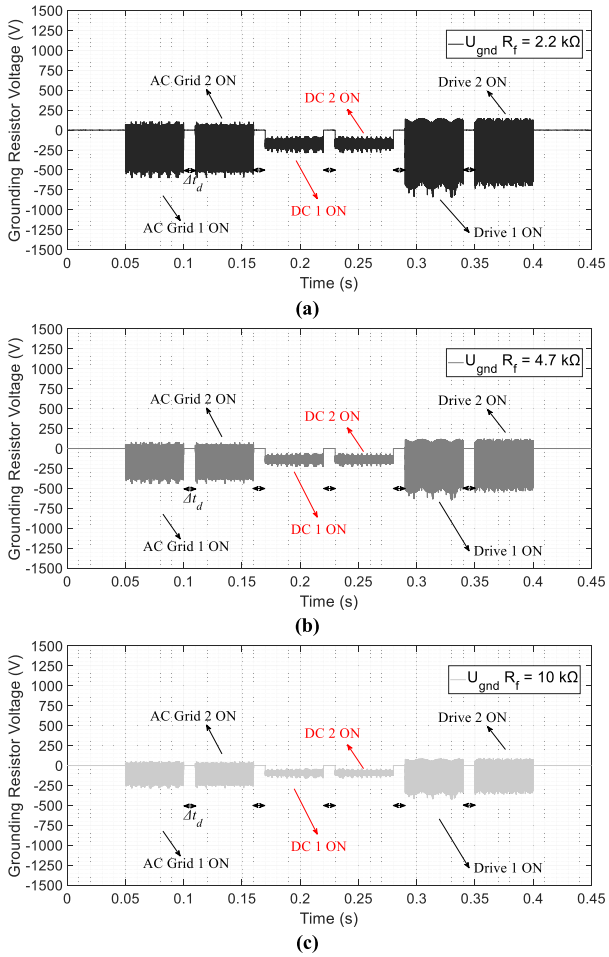

Fig. 14. DC positive pole fault in the AC grid 1 – AC drive 1 wire connection [(a): $R_f = 2.2$ kΩ; (b): $R_f = 4.7$ kΩ; (c): $R_f = 10$ kΩ].

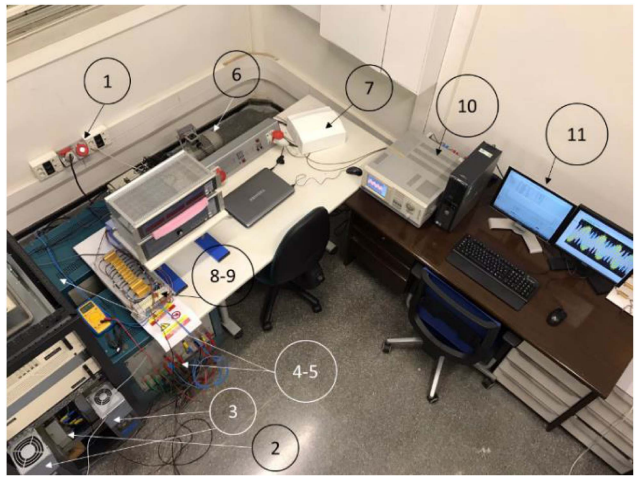

Fig. 15. Experimental setup.

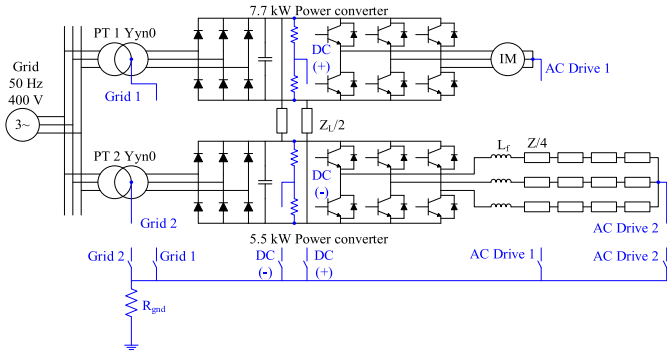

Fig. 16. Experimental electrical scheme with switchers' distribution inside (7).

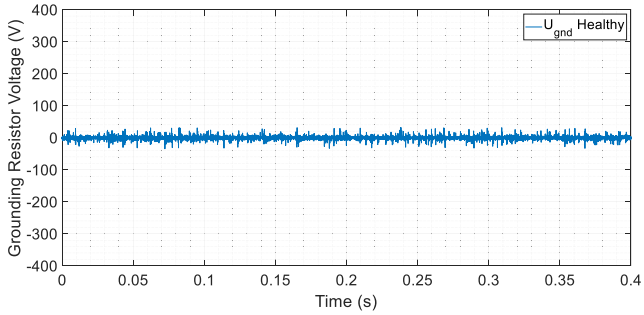

Fig. 17. Healthy state experimental test.

U_{gnd} is close to 0 V, with only high frequency components due to parasitic capacitances to ground.

This test allows to set the threshold above which the method should actuate. In this case, the maximum voltage reached by significant harmonics is 0.142 V, which corresponds to the commutation frequency.

B. Ground Fault Tests

After validating the method under a healthy state, additional tests with different faults have been carried out. Some results have been plotted in Fig. 18 to analyze method's behavior against different fault positions, whereas Fig. 19 analyzes the R_f effect. Numerical results for the faults with $R_f = 2.2$ kΩ are shown in Table I.

Fig. 18(a) presents a GF in the AC grid 1 zone (secondary of the grid 1 transformer). In this case, $f_1 = 50$ Hz harmonic components are the highest. As it can be seen, the first commutation position corresponds to the zone in fault. It has lower harmonic components than the AC grid 2 or DC commutation positions, which present a higher content in 3rd grid harmonic (150 Hz). It is caused by the non-controlled rectifier implication in the fault circuit. Analogously, an AC grid 2 fault will present lower 3rd harmonic content for its commutation position than AC grid 1.

Since in all the positions the DC component has negative polarity, a positive DC pole fault can be detected in Fig. 18(b). Nevertheless, only DC 1 and DC 2 positions have a low harmonic content. On the contrary, faults in the DC negative pole will have positive DC component in U_{gnd}.

In Fig. 18(c) and (d), faults in the AC drive 2 and 1 sides can be seen respectively. Applying the FFT to each U_{gnd} measurement, it can be observed that the higher harmonic component appears

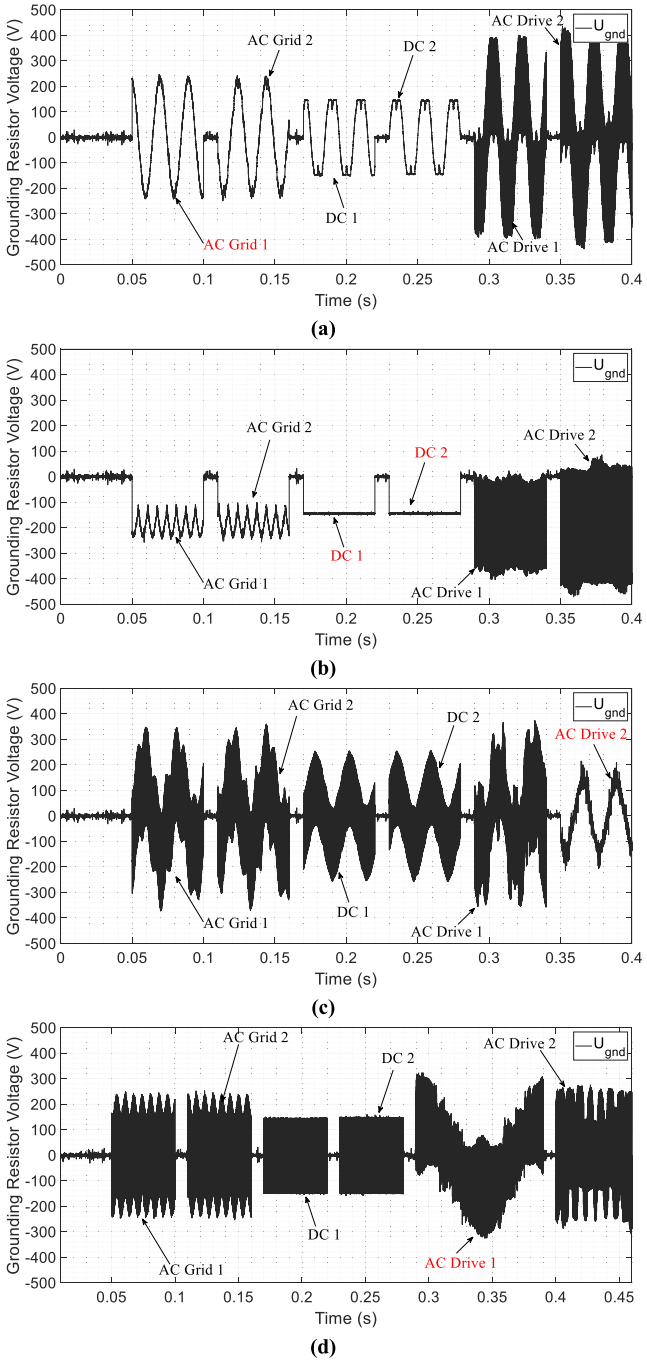

Fig. 18. U_{gnd} measurement data from experimental GF tests with $R_f = 2.2$ kΩ [(a): AC grid 1 fault; (b): DC positive pole fault in the AC grid 1 – AC drive 1 wire interconnection; (c): AC drive 2 (passive load) fault; (d): AC drive 1 (IM) fault].

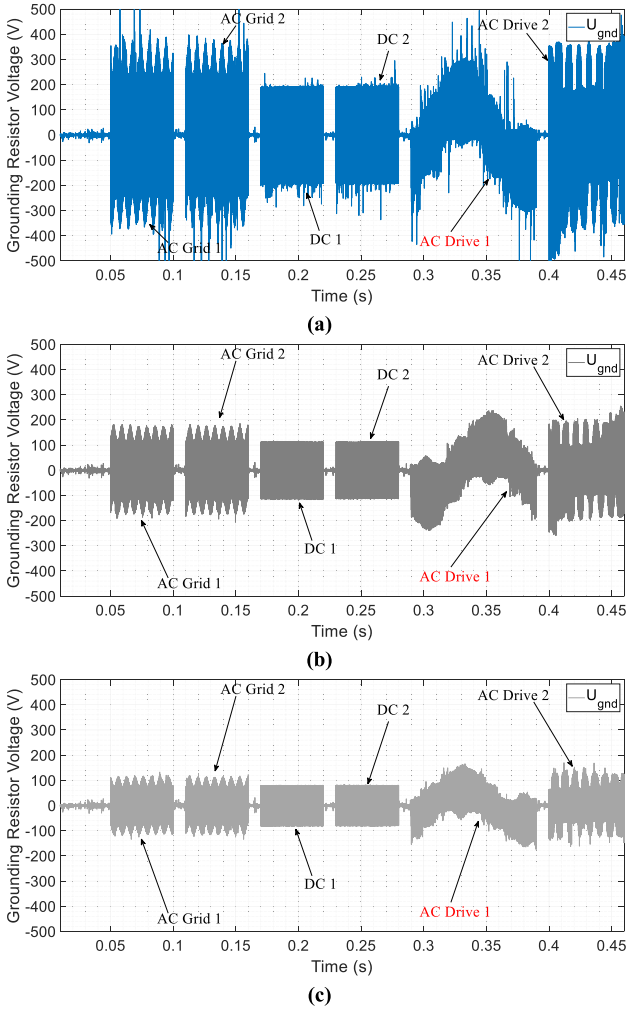

Fig. 19. Experimental tests: AC drive 1 (IM) faults [(a): $R_f = 0$ kΩ; (b): $R_f = 4.7$ kΩ; (c): $R_f = 10$ kΩ].

at the operating fundamental frequency of the drive with fault (see Table I). Nevertheless, only the commutation position where the fault is has low f_k harmonic content. For example, for a fault in the AC drive 1 (see Fig. 18(d)), harmonics with $f_{d1,1} = 10$ Hz will acquire the higher value and only the commutation in this position presents low $f_{d1,k} = 5950$ Hz component, and vice versa for AC drive 2 faults (see Fig. 18(c)).

As it can be observed in Fig. 18(d), the drive has a low operating frequency. The commutation time in this drive should be prolonged at least up to a period to have good resolution when performing the FFT. This is not a drawback since R_{gnd} limits the fault current to low values.

In order to validate the previously simulated effect of R_f, experimental tests have been carried out. In Fig. 19, tests with $R_f = 0$, 4.7 and 10 kΩ are plotted. Similar results as those obtained in the simulations have been observed in the experimental tests. Faults with low R_f increase the voltage drop in R_{gnd} while faults with low severity (high R_f) result in the opposite phenomenon. Even with $R_f = 10$ kΩ, U_{gnd} pulses still remain close to 100 V. It implies that faults can be easily detected.

The attenuation phenomenon was previously studied by authors in [29], where it was concluded that R_{gnd} and R_f conforms a voltage divider with the voltage in the fault location. As example, if a threshold of 15 V in U_{gnd} is considered, DC faults up to $R_f = 70$ kΩ can be detected according to (2) and (3).

Finally, Fig. 20 depicts the measurements of the different phase-to-neutral voltages in the AC drive 2 and $U_{gnd,}$ as well

TABLE I
MAIN FREQUENCY HARMONICS RMS VALUES FOR DIFFERENT FAULTS (R_f = 2.2 kΩ)

Switch position (and main frequency)	U_{gnd} (f_0 = 0 Hz)	U_{gnd} (f_1 = 50 Hz)	U_{gnd} ($f_{d1,1}$ = 10 Hz)	U_{gnd} ($f_{d2,1}$ = 42.5 Hz)	U_{gnd} (f_3 = 150 Hz)	U_{gnd} ($f_{d1,k}$ = $f_{d2,k}$ = 5950 Hz)
AC Grid 1 fault						
AC Grid 1 (f_1)	0.26	**162.93**	0.28	0.62	**1.19**	0.01
AC Grid 2 (f_1)	0.09	**156.73**	0.42	0.13	2.91	0.12
DC 1 (f_0)	1.13	**118.59**	0.04	0.11	23.05	0.18
DC 2 (f_0)	0.18	**117.19**	0.03	0.08	22.80	0.12
AC Drive 1 (f_{d1})	0.21	**157.41**	6.78	0.32	30.56	149.49
AC Drive 2 (f_{d2})	0.17	**156.13**	0.07	1.34	30.07	70.73
DC (+) fault						
AC Grid 1 (f_1)	**-190.21**	0.19	0.03	0.01	33.86	0.13
AC Grid 2 (f_1)	**-187.08**	0.10	0.04	0.03	33.52	0.11
DC 1 (f_0)	**-145.22**	0.00	0.02	0.02	**0.01**	0.16
DC 2 (f_0)	**-144.25**	0.01	0.05	0.01	**0.01**	0.16
AC Drive 1 (f_{d1})	**-194.03**	0.04	6.87	0.03	0.41	146.23
AC Drive 2 (f_{d2})	**-189.05**	0.20	0.12	1.15	0.71	53.36
AC Drive 1 fault						
AC Grid 1 (f_1)	0.85	0.12	**31.55**	6.77	32.12	134.03
AC Grid 2 (f_1)	0.51	0.30	**31.62**	6.77	32.14	149.27
DC 1 (f_0)	2.00	0.17	**24.45**	5.24	0.12	105.35
DC 2 (f_0)	1.24	0.34	**24.45**	5.22	0.13	106.72
AC Drive 1 (f_{d1})	0.97	0.19	**32.90**	1.83	**0.24**	4.06
AC Drive 2 (f_{d2})	0.57	0.46	**32.38**	7.10	0.78	137.18
AC Drive 2 fault						
AC Grid 1 (f_1)	1.23	4.86	3.74	**85.65**	31.11	62.40
AC Grid 2 (f_1)	0.72	5.59	3.38	**86.36**	30.65	62.61
DC 1 (f_0)	0.40	4.10	2.95	**66.67**	0.28	48.32
DC 2 (f_0)	1.45	4.02	3.03	**66.58**	0.34	48.26
AC Drive 1 (f_{d1})	0.66	5.80	3.22	**89.53**	1.32	98.08
AC Drive 2 (f_{d2})	0.86	3.75	5.53	**89.25**	0.48	**1.53**

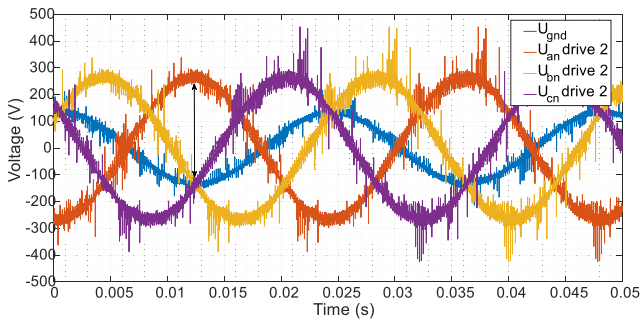

Fig. 20. AC drive 2 fault in phase "a" with $R_f = 0$ Ω: angle comparison between U_{an}, U_{bn}, U_{cn} and U_{gnd}. Experimental test.

as the AC drive 2 commutation position. Also in this case, simulation results have been physically validated. The phase in fault (in this case phase "a") is in counterphase with the U_{gnd} wave, allowing its identification.

Bearing in mind that the results of the simulations have been replicated in the performed physical tests, it can be stated that the validation has been successful. With this method GFs in microgrids with a significant presence of power electronics can be easily detected during steady state operation as R_{gnd} limits I_f.

Comparing the obtained results with the present literature, the following points can be highlighted by observing Table II. Methods that use solid grounding or LRG configurations are faster, but their capability to detect high R_f GFs is limited. In the present research, R_f max. was 10 kΩ, but GFs up to 70 kΩ could be perfectly discerned setting a threshold of $U_{gnd} = 15$ V. Furthermore, the proposed method can discern between multiple drives connected to the microgrid operating at similar or equal f_1, f_k while [10] and [12] cannot. On the same field, [26] requires of algorithm training where the proposed method not.

TABLE II
COMPARISON OF THE METHOD'S PERFORMANCE AGAINST PREVIOUS LITERATURE

Ref. no.	Detects GF		R_f max.	Diagnosis time	Grounding
	DC	AC	[kΩ]	[s]	type
[7]	✓	×	0.025	0.00125	LRG
[8]	✓	×	0	0.005	Solid
[9]	✓	×	0.001	0.0022	Solid
[10]	✓	✓	10	$1/f_{1d}$*	HRG
[12]	✓	✓	Not espec.	$1/f_{1d}$*	Solid/HRG
[13]	✓	×	Not espec.	1	Isolated
[14]	✓	×	0.002	0.0012	LRG
[17]	×	✓	23	0.020	LRG
[19]	✓	×	1	0.150	Not espec.
[25]	✓	✓	Not espec.	Not espec.	Solid
[26]	×	✓	0	0.100	HRG
Proposed method	✓	✓	***10***	***Variable** (0.450)***	***HRG***

*f_{1d}: drive fundamental frequency. **The diagnosis time depends as follows: Diag. time ≥ (No. of neutrals + midpoints)·($1/f_{1d} + \Delta t_d$), being f_{1d} the minimum frequency of the circuit; it is 0.450 s in the present research.

One of the drawbacks of this approach is the time spent in the detection process. Low operation frequencies require longer measurement times to capture at least one period of U_{gnd}, to ensure a good accuracy during the FFT process. In addition, the more neutrals and midpoints the microgrid has, the more sampling will be necessary. Despite this, the detection time does not affect to the system safety because the fault current is limited by R_{gnd}. By consequence, the microgrid could normally operate at rated conditions with a first fault. However, the time spent in the diagnosis should be the lowest possible in order to reduce the probabilities of a second GF.

Another possible disadvantage is that for a single R_{gnd} connection, long cables should be use in large microgrids to connect the resistance to all the neutrals/midpoints. Then, the method should be affected by electromagnetic interference (EMI) perturbations. Furthermore, the high frequency components used by the method could be attenuated with these distances. The experimental tests have been done in an small microgrid, where the proposed topology runs satisfactorily. However, to avoid these adverse effects for the method in large microgrids, each neutral/midpoint R_{gnd} and own commutation element should be grounded. After, each part of each grounding, including the U_{gnd} voltmeter, must be communicated with a master system that coordinates the sequence of switchers. The communication should be preferably done with optical fiber as it is fast and unaffected by EMI effects.

VII. CONCLUSION

This paper presents a ground faults detection method for microgrid that sequentially connects and disconnects a ground

resistor among the different neutrals and midpoints. The method allows the fault detection and zone identification by examining the frequency spectra of the voltage measurement in the grounding resistor where most of commercial protection relays fail. With this method, the circulating currents among different grounded points are not a problem and the analysis can be performed in steady-state operation due to the high-impedance grounding of the system.

The method presents satisfactory results for AC and DC sides fault recognition even if two or more AC sides have the same settings. Furthermore, it is able to detect high resistance faults. The faulty phase (in AC side case) is discerned by measuring the phase-to-neutral voltages, and by examining the voltage polarity, the faulty pole can be located in case of DC fault.

To corroborate the method, simulations and experimental tests have been carried out, obtaining satisfactory results in a four node DC microgrid with two AC grid interconnections and two controlled AC drives. The faulty zone can be easily identified in both scenarios at steady-state conditions, and no damages were observed during experimental tests.

The method has correctly worked detecting the faulty zone. It could help to isolate the affected area and continue operating (if possible) with the rest of the system. However, it also has some weakness. For example, the switching times of the grounding commutation positions will be time-extended if the fundamental frequency of the drive in fault is low, as at least one period should be recorded to perform an accurate FFT on U_{gnd}. Additionally, faults in the DC zone can be detected, but they cannot be located. This is because R_f and R_{gnd} assume most of the voltage drop in the fault circuit, while only a negligible portion occurs in the cable impedance. This last fact leads the doors open to further investigations, which could focus on designing new methods to locate faults in DC after the detection. Another further work should be focused on the application of this method for large distance microgrids by grounding each neutral/midpoint and by implementing communication systems among them.

REFERENCES

[1] S. Ferahtia et al., "Optimal control and implementation of energy management strategy for a DC microgrid," *Energy*, vol. 238, 2022, Art. no. 121777.

[2] IEA, "Global EV outlook 2021," International Energy Agency, IEA, Paris, April, 2021.

[3] P. Bojek and H. Bahar, "Renewable power," International Energy Agency, IEA, Paris, Nov. 2021.

[4] D. F. Kavanagh, K. N. Gyftakis, and M. D. McCulloch, "Early-onset degradation of thin-film magnet wire insulation for electromechanical energy converters," in *Proc. IEEE 12th Int. Symp. Diagn. Elect. Mach., Power Electron. Drives*, 2019, pp. 37–43.

[5] C. S. Mardegan and R. Rifaat, "Insights into applications of IEEE standards for ground-fault protection in industrial and commercial power systems," *IEEE Trans. Ind. Appl.*, vol. 51, no. 4, pp. 2854–2861, Jul./Aug. 2015.

[6] J. Mohammadi, F. Badrkhani Ajaei, and G. Stevens, "Grounding the DC microgrid," *IEEE Trans. Ind. Appl.*, vol. 55, no. 5, pp. 4490–4499, Sep./Oct. 2019.

[7] R. Bhargav, B. R. Bhalja, and C. P. Gupta, "Novel fault detection and localization algorithm for low-voltage DC microgrid," *IEEE Trans. Ind. Informat.*, vol. 16, no. 7, pp. 4498–4511, Jul. 2020.

[8] D. Salomonsson, L. Soder, and A. Sannino, "Protection of low-voltage DC microgrids," *IEEE Trans. Power Del.*, vol. 24, no. 3, pp. 1045–1053, Jul. 2009.

[9] Z. Zhang, Q. Chen, R. Xie, and K. Sun, "The fault analysis of PV cable fault in DC microgrids," *IEEE Trans. Energy Convers.*, vol. 34, no. 1, pp. 486–496, Mar. 2019.

[10] J. M. Guerrero, G. Navarro, K. Mahtani, and C. A. Platero, "Ground fault detection method for variable speed drives," *IEEE Trans. Ind. Appl.*, vol. 57, no. 3, pp. 2547–2558, May/Jun. 2021.

[11] J. M. Guerrero, G. Navarro, K. Mahtani, and C. A. Platero, "AC drive side ground fault location for DC/AC systems based on AC phases and grounding resistor voltages," *IEEE Trans. Ind. Appl.*, vol. 58, no. 3, pp. 3567–3577, May/Jun. 2022.

[12] T. Gruhn, J. Glenney, and M. Savostianik, "Type B ground-fault protection on adjustable frequency drives," *IEEE Trans. Ind. Appl.*, vol. 54, no. 1, pp. 934–939, Jan./Feb. 2018.

[13] J. Park, "Ground fault detection and location for ungrounded DC traction power systems," *IEEE Trans. Veh. Technol.*, vol. 64, no. 12, pp. 5667–5676, Dec. 2015.

[14] P. Chauhan, C. P. Gupta, and M. Tripathy, "High speed fault detection and localization scheme for low voltage DC microgrid," *Int. J. Elect. Power Energy Syst.*, vol. 146, 2023, Art. no. 108712.

[15] L. Xu et al., "A review of DC shipboard microgrids—Part II: Control architectures, stability analysis, and protection schemes," *IEEE Trans. Power Electron.*, vol. 37, no. 4, pp. 4105–4120, Apr. 2022.

[16] Y. Zhou, C. Ji, Z. Dong, and S. Zhang, "Cooperative control of SFCL and SMES-battery HESS for mitigating effect of ground faults in DC microgrids," *IEEE Trans. Appl. Supercond.*, vol. 31, no. 8, Nov. 2021, Art. no. 5403305.

[17] Y. Du et al., "Single line-to-ground faulted line detection of distribution systems with resonant grounding based on feature fusion framework," *IEEE Trans. Power Del.*, vol. 34, no. 4, pp. 1766–1775, Aug. 2019.

[18] M. Karmacharya and R. Gokaraju, "Fault location in ungrounded photovoltaic system using wavelets and ANN," *IEEE Trans. Power Del.*, vol. 33, no. 2, pp. 549–559, Apr. 2018.

[19] X. Wang, R. Wang, Y. Liu, and X. Gao, "Impedance ground faults detection and classification method for DC microgrid," *J. Elect. Eng. Technol.*, vol. 18, no. 6, pp. 4011–4023, Mar. 2023.

[20] D. K. J. S. Jayamaha, N. W. A. Lidula, and A. D. Rajapakse, "Wavelet-multi resolution analysis based ANN architecture for fault detection and localization in DC microgrids," *IEEE Access*, vol. 7, pp. 145371–145384, 2019.

[21] J. Yang, S. B. Lee, J. Yoo, S. Lee, Y. Oh, and C. Choi, "A stator winding insulation condition monitoring technique for inverter-fed machines," *IEEE Trans. Power Electron.*, vol. 22, no. 5, pp. 2026–2033, Sep. 2007.

[22] J. Zheng, Z. Wang, D. Wang, B. Wang, and M. Li, "Diagnostic strategy and modeling of PMSM stator winding fault in electric vehicles," in *Proc. IEEE Chin. Automat. Congr.*, 2017, pp. 3870–3874.

[23] S. B. Lee et al., "Condition monitoring of industrial electric machines: State of the art and future challenges," *IEEE Ind. Electron. Mag.*, vol. 14, no. 4, pp. 158–167, Dec. 2020.

[24] M. Riera-Guasp, J. A. Antonino-Daviu, and G.-A. Capolino, "Advances in electrical machine, power electronic, and drive condition monitoring and fault detection: State of the art," *IEEE Trans. Ind. Electron.*, vol. 62, no. 3, pp. 1746–1759, Mar. 2015.

[25] J. Hu, L. Wei, J. McGuire, and Z. Liu, "Faulted phase location identification for adjustable speed drives in high-resistance grounding system," *IEEE Trans. Ind. Appl.*, vol. 54, no. 5, pp. 4457–4463, Sep./Oct. 2018.

[26] Z. Chen et al., "A data-driven ground fault detection and isolation method for main circuit in railway electrical traction system," *ISA Trans.*, vol. 87, pp. 264–271, Apr. 2019.

[27] J. M. Guerrero et al., "Ground fault detection method for DC microgrids based on switching grounding connections," in *Proc. IEEE Int. Conf. Environ./Elect. Eng. IEEE Ind. Commercial Power Syst. Europe*, 2023, pp. 1–7.

[28] J. M. Guerrero, C. A. Platero, D. Serrano-Jiménez, V. Valiño, and P. Pomares, "Ground fault localizer for an electric circuit, electric circuit and ground fault location method," Spanish Patent 2930209 A1, Oficina Española de Patentes y Marcas, Madrid, Spain, Dec. 07, 2022.

[29] J. M. Guerrero, G. Navarro, C. A. Platero, P. Tian, and F. Blázquez, "A novel ground fault detection method for electric vehicle powertrains based on a grounding resistor voltage analysis," *IEEE Trans. Ind. Appl.*, vol. 56, no. 5, pp. 4934–4944, Sep./Oct. 2020.

José Manuel Guerrero (Member, IEEE) was born in Madrid, Spain, in 1996. He received the B.E. degree in energy resources, fuels and explosive engineering, the M.E. degree in electrical engineering and the Ph.D. degree in electrical engineering from the Universidad Politécnica de Madrid, Madrid, in 2018, 2019, and 2022, respectively. From 2020 to 2023, he was an Assistant Professor with the Department of Energy and Fuels, Universidad Politécnica of Madrid. In 2023, he was a Lecturer and Researcher with the Electronics and Computing Department, Mondragon Unibertsitatea, Mondragón, Spain. He is currently a Researcher Associate Professor with the Electrical Department of the Universidad del País Vasco, where he researches about diagnosis and protections of electric power systems and electrical machines.

Itxaso Aranzabal received the B.Sc. degree in industrial electronic engineering and the M.Sc. degree in automatization and insdustrial electronic engineering from the University of Deusto, Bilbao, Spain, in 2003 and 2010, respectively, and the Ph.D. degree from the University of the Basque Country, Bilbao, in 2019. From 2007 to 2012, she was an Engineer with Consulting, Engineering and Architecture companies. In 2017, she started teaching with the Electrical Engineering Department, University of the Basque Country, Bilbao.

Julen Gómez-Cornejo received the qualifications of Electronic Engineer, master's degree in advanced electronic systems, and the Ph.D. degree in electronics and telecommunications from the University of the Basque Country UPV/EHU, Bilbao, Spain, in 2010, 2012, and 2018, respectively. From 2007 to 2010, he was an Assistant Professor with the different departments of the University of the Basque Country UPV/EHU. In 2016, he started with the Electrical Engineering Department, University of the Basque Country as an Assistant Professor and a Researcher.

Pablo Eguía (Member, IEEE) was born in Bilbao, Spain, in 1973. He received the Ph.D. degree in electrical engineering from the University of the Basque Country, Bilbao, in 2007. He is currently an Assistant Professor with the Department of Electrical Engineering, University of the Basque Country UPV/EHU, Bilbao. He is the Leader of GISEL research group. His research interests include power systems analysis and simulation, integration of renewable generation, and power system control and protection.

Sergio Zarate was born in Vitoria-Gasteiz, Spain. He received the B.Sc., M.Sc. and Ph.D. degrees in electrical engineering from Mondragon Unibertsitatea, Mondragon, Spain, in 2012, 2014, and 2018, respectively. Since 2018, he has been with the Electronics Department of the Faculty of Engineering, Mondragon Unibertsitatea, Mondragón, Spain, where he is currently a Lecturer and Researcher. His research interests include drives, electrical machines vibration and permanent magnet machine design, optimization and diagnosis.

Carlos A. Platero (Senior Member, IEEE) was born in in Madrid, Spain, in 1972. He received the Dipl. and Ph.D. degrees in electrical engineering from the Universidad Politécnica de Madrid, in 1996 and 2007, respectively. From 1996 to 2008, he was with ABB Generación S.A., Alstom Power S.A. and ENDESA Generación S.A., always involved in the design and commissioning of power plants. In 2002, he began teaching with the Electrical Engineering Department, Universidad Politécnica de Madrid and joined an energy research group. In 2008, he became a Full-time Associate Professor.